

The pore-network-continuum modeling of two-phase flow properties for multiscale digital rocks

Bowen Shi^a, Jianqi Rong^a, Han Jiang^{a,b,*}, Bo Guo^c, S. Majid Hassanzadeh^{a,b,d}, Chao-Zhong Qin^{a,b,*}

^a School of Resources and Safety Engineering, Chongqing University, 400044, Chongqing, China

^b State Key Laboratory of Coal Mine Disaster Dynamics and Control, Chongqing University, 400044, Chongqing, China

^c Department of Hydrology and Atmospheric Sciences, University of Arizona, Tucson, AZ 85721, USA

^d Department of Earth Sciences, University of Utrecht, P.O. Box 80021, 3508 TA, Utrecht, Netherlands

ARTICLE INFO

Keywords:

Multiscale porous media
Digital rocks
Pore-network-continuum model
Two-phase flow
Microporosity
Relative permeability

ABSTRACT

Many subsurface formations and reservoirs exhibit multiscale and heterogeneous pore structures, such as soils, carbonate rocks, shales and tight sandstones. Understanding and predicting their two-phase flow properties are crucial to underground applications including contamination remediation, oil and gas recovery, and geological storage of carbon dioxide. For a multiscale digital rock, pores with a wide pore-size distribution spanning several orders of magnitude cannot be visualized in one image, due to the trade-off between image resolution and field of view. However, a large number of unresolved pores (i.e. microporosity) can challenge the modeling of flow and transport. We develop an efficient pore-network-continuum model (PNCM) for quasi-static two-phase flow in multiscale digital rocks. The resolved pores and microporosity are represented by a pore network and continuum grids, respectively. Instead of costly CT-based characterization, we propose to use the bimodal van Genuchten model of mercury intrusion capillary pressure to infer the pore-size distribution of heterogeneous microporosity. The PNCM is applied to a laminated sandstone with synthesized homogeneous microporosity and an Estailades carbonate rock with heterogeneous microporosity. Both single-phase and two-phase flow properties including absolute permeability, formation factor, resistivity index, capillary pressure, and relative permeability are predicted and compared with experimental data. The good agreement demonstrates the robustness and reliability of the developed PNMC. Using the case studies, we illustrate how microporosity influences and determines two-phase flow properties.

1. Introduction

Flow and transport in porous media play a critical role in many industrial and subsurface applications such as fuel cells (Niblett et al., 2020), underground storage of CO₂ and H₂ (Wang et al., 2014; Feldmann et al., 2016; Hefny et al., 2020), groundwater contamination (Brusseau et al., 2021), and hydrocarbon extraction (Morel et al., 1997). To numerically predict or even optimize flow and transport in those applications, two-phase flow properties (e.g., relative permeability and capillary pressure) are of great importance.

With the advancement of non-destructive imaging technique and computation power, digital rock analysis has proven to be a powerful tool for comprehensive understanding of multiphase flow at the pore scale (Blunt et al., 2013; Aghaei and Piri, 2015; Sadeghnejad et al., 2021;

Wang et al., 2021; Qin et al., 2022). Usually, pore spaces are segmented from the digital image of a rock sample, and then pore-scale numerical models, such as direct numerical simulations (DNS) and pore-network models (PNMs), are developed to predict flow properties.

For a porous rock with unimodal pore-size distributions (PSD), selecting an appropriate imaging resolution is straightforward. This ensures adequate capture of pore-space geometrical details within a representative elementary volume (REV), yielding satisfactory consistency between simulated and measured flow properties (Piller et al., 2009; Saxena et al., 2017). However, for rock samples with multiscale pore structures such as carbonate rocks, tight sandstones and mudstones, their pore sizes are widely distributed across multiple orders of magnitude from a few nanometers to hundreds of micrometers (Bijeljic et al., 2013; Pak et al., 2016; Liu et al., 2017; Dai et al., 2023). As a

* Corresponding authors:

E-mail addresses: hanjiang@cqu.edu.cn (H. Jiang), chaozhong.qin@cqu.edu.cn (C.-Z. Qin).

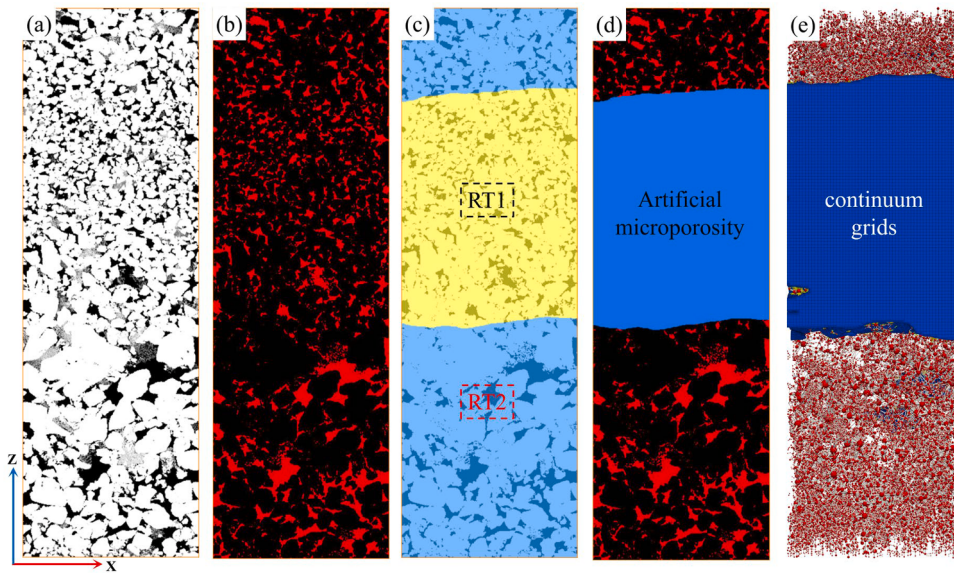


Fig. 1. The demonstration of the synthesis of a multiscale digital rock. (a) The 2D slice of the ANLEC sandstone with a size of 1400×450 voxels and a voxel resolution of $10.34 \mu\text{m}$. (b) The binary image where the red and black represent resolved pores and solid. (c) The rock-type distribution map generated by the Minkowski functionals. (d) The ternary image by the combination of (b) and (c), where the RT1 region has been replaced by the blue artificial microporosity. (e) The computational mesh for the pore-network-continuum model, consisting of continuum grids for RT1 and the pore network for RT2.

result, due to the trade-off between image resolution and field of view, small pores cannot be resolved in a single scanning image. The voxels in the digital tomogram that contain unresolved pores constitute sub-domains (referred to as microporosity) that cannot be neglected (Bauer et al., 2011). Microporosity causes great challenges for numerical approaches, and induces deviations from standard models of two-phase flow (Soulaine et al., 2016; Sun and Torres-Verdín, 2022). Therefore, it is essential to develop numerical models capable of accounting for flow behaviours across different scales of pore structures, and to investigate the influence of microporosity on two-phase flow properties.

Up to now, there have been two numerical approaches for simulating two-phase flow in multiscale porous media. One is the micro-continuum approach based on the Darcy-Brinkman-Stokes (DBS) equation (Carrillo et al., 2020, 2022), and another is the multiscale pore-network approach which represents microporosity by either a fine pore network (Jiang et al., 2013; Mehmani and Prodanović, 2014; Prodanović et al., 2014) or a Darcy-scale pore network (Bauer et al., 2012; Ruspini et al., 2021), or micro-links (Bultreys et al., 2015; 2016a; 2016b; Foroughi et al., 2024). Carrillo et al. (2020) developed a two-phase micro-continuum model (MCM) which couples the volume of fluid (VOF) method for flow in resolved pores and the two-phase Darcy model for flow in microporosity. Later on, they used the model to study the effects of microporosity on two-phase flow properties, such as absolute permeability, fluid breakthrough time, residual saturation, and relative permeability (Carrillo et al., 2022). However, due to high computational efforts, it is still prohibitive to simulate REV-size porous media with the micro-continuum approach. The multiscale pore-network approach presented here is computationally efficient. Mehmani and Prodanović (2014) constructed two-scale pore networks to investigate the impact of grain-filling and pore-filling microporosity on two-phase flow properties. Bultreys et al. (2016a) performed quasi-static two-phase flow simulations of five multiscale rock samples by micro-links, finding that connectivity and wettability significantly influence relative permeability and residual saturation. Ruspini et al. (2021) proposed a workflow for estimating flow properties of Darcy-scale pore networks, and successfully predicted capillary pressure and relative permeability of multiscale sandstones and carbonate rocks. However, to the best of our knowledge, the multiscale pore-network approach cannot explicitly consider the large number of micropores that are encountered in real

porous medium like carbonate rocks. Moreover, due to the coarse representation of microporosity by a Darcy-scale pore network, heterogeneity of microporosity can be smeared, and thus substantially impacts numerical predictions (Zhao et al., 2025).

To balance computational efficiency and accuracy, Zhang et al. (2024) proposed a numerical framework for pore-network-continuum modeling of flow and transport in multiscale porous media. Compared with the multiscale pore-network modeling, microporosity is represented by image voxels as in DBS-based models, to consider highly heterogeneous microporosity. To further reduce computational efforts, Shi et al. (2024) developed a multilevel controllable coarsening algorithm for microporosity voxels, and around 90 % of microporosity voxels can be merged to larger computational grids. The pore-network-continuum models (PNCMs) have been developed for single-phase flow and transport (Zhang et al., 2024), and validated against experimental data (Shi et al., 2024). However, the framework has not yet been generalized to two-phase flow in multiscale porous media.

In the present work, we develop a quasi-static two-phase PNCM, to investigate drainage and imbibition flow properties of multiscale porous media, including resistivity index, capillary pressure and relative permeability. Compared to the single-phase PNCM (Shi et al., 2024) and traditional pore-network models (Dong and Blunt, 2009), our quasi-static two-phase PNCM holds three new features. First, for a continuum-scale microporosity grid, we introduce the concept of percolation pressure, at which the non-wetting phase breaks through the microporosity grid and starts to invade neighboring grids. Second, we use the Land trapping model (Land, 1968) and the Killough hysteresis model (Killough, 1976) to account for the hysteresis of capillary pressure and relative permeability of microporosity grids. Last but not least, based on mercury intrusion capillary pressure (MICP) data, we use the bimodal van Genuchten model (Durner, 1994) to characterize the pore-size distribution of heterogeneous microporous domain. Our approach does not require expensive CT-based characterization of microporosity (Wang et al., 2022), rather it only needs a MICP curve, and can eliminate additional data fittings of microporosity properties. Two realistic rock samples are used in the case studies, i.e., a laminated sandstone with synthesized homogeneous microporosity, and an Estallades carbonate rock of a bimodal pore-size distribution and

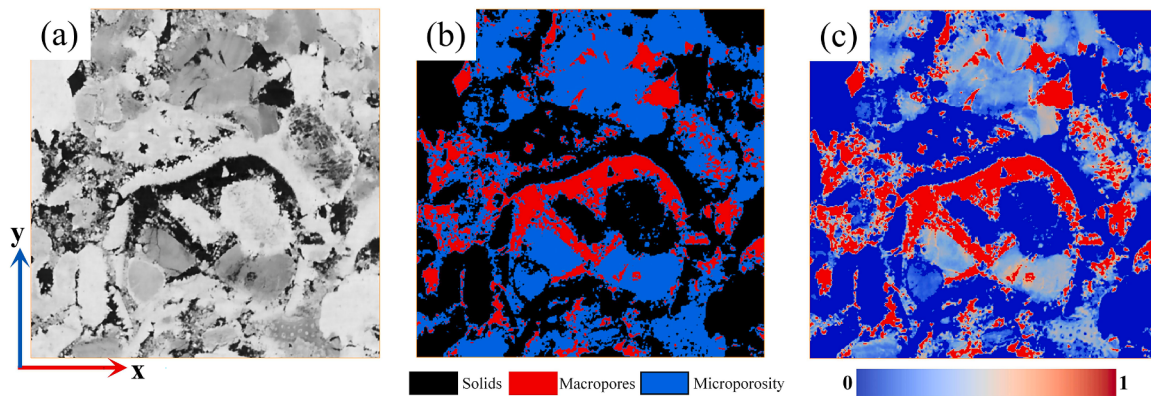


Fig. 2. (a) The 2D slice of Estaillades carbonate rock with a size of 400^3 voxels and a voxel size of $6.2 \mu\text{m}$. (b) The ternary image obtained by threshold segmentation. The red, blue and black represent the resolved pores, microporosity and solid, respectively. (c) The porosity map obtained by normalization, where 0, 1, and the values between correspond to solid, resolved pores, and microporosity, respectively.

heterogeneous microporosity. The predicted two-phase flow properties for the laminated sandstone are compared with those by a full-scale PNM. For the Estaillades carbonate rock, the numerical results are compared with experimental data in the open literature. We aim to validate the developed model for predicting two-phase flow properties of multiscale porous media, and to illustrate the influence of microporosity on these properties.

2. Materials and methods

2.1. Rock samples and computational grids

In the present work, two multiscale digital rocks with distinct microporosity characteristics are used. The first one is re-produced from a sandstone sample with layered pore structures, provided by Australian Carbon Capture and Storage Research Centre (ANLEC). The original CT image of the ANLEC sandstone was obtained from Jiang and Arns (2021), which has the size of $2800 \times 900 \times 900$ voxels with a voxel size of $5.17 \mu\text{m}$. To reduce computational efforts, we reduced the original image resolution by half, as shown in Fig. 1(a). Then, the solid phase and pore spaces were segmented by a manual threshold, yielding the binary image in Fig. 1(b). To synthesize a multiscale digital rock, we utilized

the Minkowski functionals to extract structural feature parameters (e.g., volume, surface area, integral of mean curvature, integral of total curvature), and classified the regions with similar pore geometries by machine learning algorithms (Jiang and Arns, 2020). As illustrated in Fig. 1(c), the blue and yellow regions are termed as rock-type 1 (RT1) and rock-type 2 (RT2), respectively. Subsequently, we masked the pore-scale details of the RT1 domain, and replaced it with a homogeneous monolithic microporous domain. The final ternary image is shown in Fig. 1(d), where the black, red and blue represent solid, resolved pores and microporosity, respectively. Finally, the synthesized multiscale digital rock includes about 2.8 million voxels of resolved pores in RT2 domain and about 12.4 million voxels of microporosity. By using the coarsening algorithm in (Shi et al., 2024), as shown in Fig. 1(e), the computational mesh is composed of a pore network of 30,157 pore bodies and 824,405 continuum grids. To verify the two-phase PNCM, we compare its predictions against the full-scale pore-network modeling of the sandstone.

The second digital rock is from the well-known Estaillades carbonate, extensively used in the development and validation of multiscale numerical models. The raw scanning images and experimentally measured flow properties used in this work were made publicly available by Bultreys et al. (2015) on the Digital Porous Media Portal (<https://digitalporousmedia.org/published-datasets/>). This dataset is highly

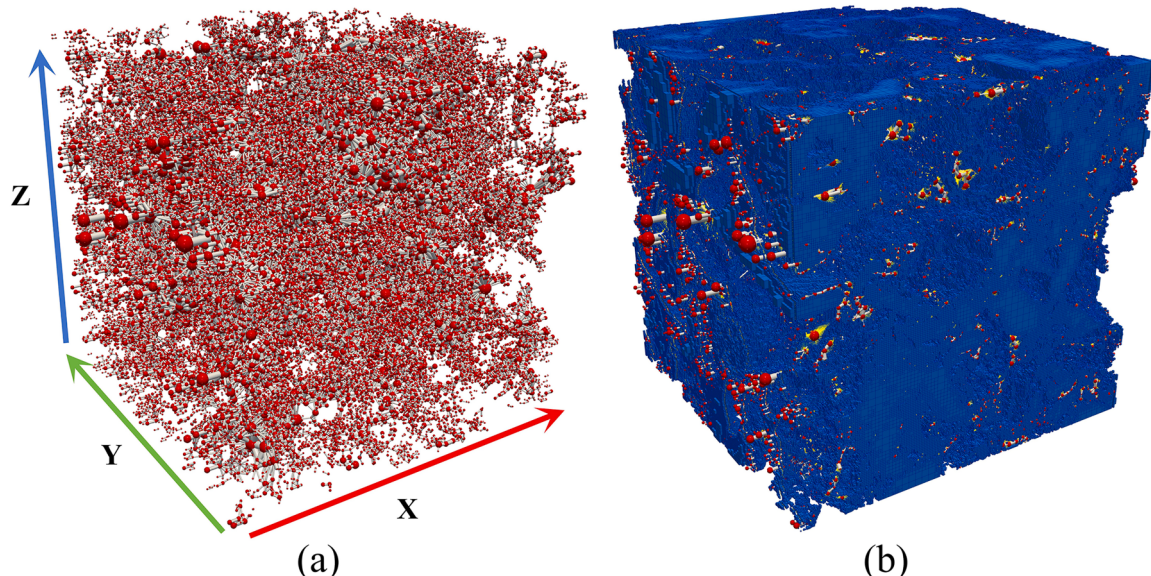


Fig. 3. (a) The pore network of the resolved pores for the Estaillades carbonate rock. (b) The multiscale computational mesh for the two-phase PNCM by the algorithm developed in Shi et al. (2024).

suitable for testing our model, as the grayscale of voxels is linearly correlated with their unresolved pore content. We first extracted a subdomain with a size of $800 \times 800 \times 800$ voxels and a voxel size of $3.1 \mu\text{m}$ from the center of the original image. To reduce computational efforts, the image resolution of subsample was then reduced by half, resulting in the coarsened image with the size of $400 \times 400 \times 400$ voxels and the voxel size of $6.2 \mu\text{m}$, as shown in Fig. 2(a). The voxels are classified as non-porous solid, resolved pores, and microporosity by a multi-threshold segmentation as illustrated in Fig. 2(b). The segmented ternary image contains 11.7 % resolved pore voxels and 41.0 % microporosity voxels, which is well consistent with those of the high-resolution original image (i.e., 11.8 % resolved pore voxels and 40.7 % microporosity voxels). Fig. 2(c) shows the porosity map of a 2D slice, which was obtained by normalizing the grayscale values of microporosity voxels using the difference between the average CT values of the resolved pores and solid phase (Zhao et al., 2025). The total porosity of the coarsened image is 25.5 %, which is almost the same as the experimental value of 25 %. We used the same algorithm as for the ANLEC sandstone to generate the computational mesh for the Estaillades carbonate rock, which comprises 85,414 pore bodies and approximately 7.6 million microporosity grids as shown in Fig. 3. The experimental results from (Han et al., 2007; Bauer et al., 2012; Bultreys et al., 2015; Ott et al., 2015), including absolute permeability, formation factor, resistivity index curve, capillary pressure and relative permeability curves, were used to validate the two-phase PNCM.

2.2. Flow properties of microporosity

For reservoir cores with similar diagenesis, despite heterogeneous porosity and entry-pressure radius in the microporous domain, their pore structures exhibit similarity. Based on this assumption, we use porosity (φ), entry-pressure radius (r), and empirical equations/models including Archie's model, van Genuchten (VG) equation, Katz-Thompson (K-T) equation, Land and Killough hysteresis models to characterize average flow properties of reference microporosity (Archie, 1942; Land, 1968; Killough, 1976; van Genuchten, 1980; Katz and Thompson, 1986, 1987) and to map these properties to heterogeneous microporosity. The average flow properties we consider include absolute permeability (k), formation factor (F), resistivity index curve ($RI(s^w)$), capillary pressure curve ($P_c(s^w)$) and relative permeability curves ($k_r(s^w)$), all of which can be derived from numerical simulations of a representative subvolume of microporosity by a classical PNM.

For a real multiscale rock, the porosity map can be derived from the grayscale values of microporosity in the CT image (Bultreys et al., 2015) or the differential analysis between the dry and saturated CT images (Wang et al., 2022). The entry-pressure radius, which is the largest pore radius for non-wetting intrusion into a microporosity element/grid, can

be determined by the Young-Laplace equation:

$$r = \frac{2\sigma\cos\theta}{P_e} \quad (1)$$

where σ is the interfacial tension, θ is the static contact angle, and P_e is the capillary entry pressure for each microporosity grid. P_e may be obtained by fitting the Brooks-Corey model from capillary pressure-saturation data points of each microporosity voxel, measured directly from quasi-static drainage experiments combined with in-situ CT scanning (Wang et al., 2022). However, this experimental approach is time-consuming and labor-intensive. Alternatively, we propose a simplified workflow to assign an entry-pressure radius to each microporosity grid, based on the dual-pore-size distribution derived from the MICP curve. The implementation detail for the Estaillades carbonate rock can be seen in Appendix A.

Once the distributions of porosity and entry-pressure radius for microporosity grids are determined, the absolute permeability of each grid can be estimated by the K-T equation (Katz and Thompson, 1986, 1987):

$$k = \frac{\varphi r^2}{32\tau} \quad (2)$$

where τ is the tortuosity of microporosity and can be estimated through image analysis or numerical simulations (Fu et al., 2021). The formation factor of a fully saturated microporosity grid can be described by the Archie's law:

$$F = \frac{\sigma_w}{\sigma_o} = \varphi^m \quad (3)$$

where m is the cementation exponent. Meanwhile, electrical resistivity of a partially saturated microporosity grid can be expressed by the Archie's saturation equation (Archie, 1942):

$$RI = (s^w)^{-n} \quad (4)$$

where n is the saturation exponent.

Capillary pressure and relative permeability curves are modeled by the VG model (van Genuchten, 1980). The hysteresis between drainage and imbibition processes is modeled by the Land and Killough models (Land, 1968; Killough, 1976). The details are presented in Section 2.3.1 and Section 2.3.2.

2.3. Quasi-static two-phase pore-network-continuum model

For the quasi-static PNCM, the traditional invasion-percolation theory, which assumes flow in porous media as an infinitely slow process

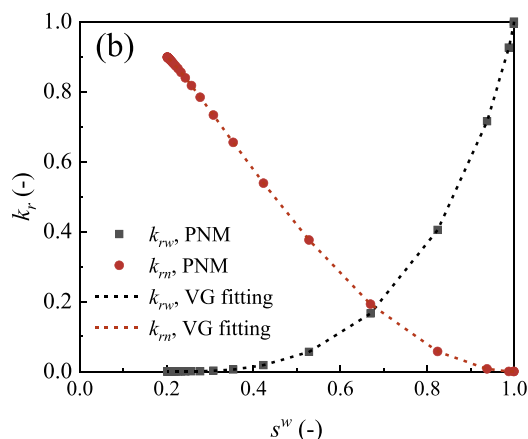
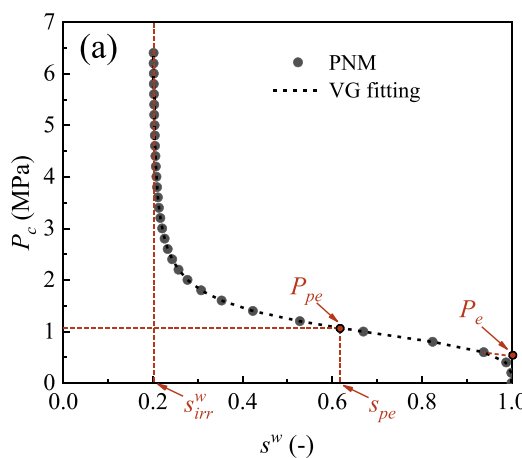


Fig. 4. Schematic of (a) the capillary pressure curve and (b) the relative permeability curve of representative microporosity for the primary drainage.

with negligible viscous forces, is employed. We describe the PNCM for the primary drainage and main imbibition processes in Sections 2.3.1 and 2.3.2, respectively. After determining the distribution of wetting and non-wetting phases in the multiscale domain at a given capillary pressure, we introduce the calculations of relative permeability and resistivity index in Section 2.3.3.

2.3.1. Primary drainage process

In the primary drainage, resolved pores and microporosity are initially saturated with the wetting phase. We increase the pressure of non-wetting fluid phase at the inlet boundary with small increments. As a result, the nonwetting phase gradually invades the network.

The cross-sections of pore bodies and pore throats of resolved pores are geometrically simplified into triangles, squares, and circles, according to their shape factors (Mason and Morrow, 1991). According to the geometric information of pore elements, capillary entry pressures are estimated by the MS-P theory (Patzek, 2001). In invaded non-circular pore bodies and pore throats, wetting phase remains at corners, leading to an apparent increase in the connectivity of wetting phase. After determining the local saturation of each pore element, the conductivity of wetting and non-wetting phases can be calculated following (Hefny et al., 2020).

For each microporosity grid, its capillary entry pressure, percolation pressure, capillary pressure curve, and relative permeability curve are obtained as follows:

- (1) Obtaining two-phase flow properties of microporous subdomain. The quasi-static PNM is used to simulate the drainage and imbibition processes in microporous subdomain. A representative pore network of microporous subdomain may be extracted from high-resolution scanning images or may be numerically generated based on the pore-size distribution from MICP (Idowu and Blunt, 2009). In this work, we use the former method to obtain flow properties of microporous subdomain in ANLEC sandstone, while microporosity properties of Estaillades carbonate adopted from (Bultreys et al., 2016a) were obtained by the latter method. Fig. 4 shows typical capillary pressure and relative permeability curves. These curves are provided for demonstration purposes and are not based on an actual rock sample.
- (2) Fitting the empirical coefficients of constitutive or empirical equations. The VG model is used to fit the simulated capillary pressure and relative permeability curves (van Genuchten, 1980):

$$s_e^w = [1 + (\alpha P_c)^N]^{-M} \quad (5)$$

$$k_r^w(s_e^w) = (s_e^w)^\kappa \left[1 - \left(1 - s_e^{w(1/M)} \right)^M \right]^2 \quad (6)$$

$$k_r^n(s_e^w) = (1 - s_e^w)^\zeta \left[1 - s_e^{w(1/M)} \right]^{2M} \quad (7)$$

where P_c is the capillary pressure, α [1/L] is the fitting coefficient related to the invasion capillary pressure, N is the dimensionless coefficient related to the PSD, M is given as $M = 1 - 1/N$, κ and ζ are the fitted coefficients, and s_e^w is the effective saturation of wetting phase defined as:

$$s_e^w = \frac{s^w - s_{ir}^w}{1 - s_{ir}^w} \quad (8)$$

where s^w is the actual wetting saturation and s_{ir}^w is the irreducible wetting phase saturation. Note that the wetting relative permeability curve is normalized by the absolute permeability, while the non-wetting phase relative permeability curve is normalized by the non-wetting phase permeability at the end of the primary drainage.

(1) Determining capillary pressure curves for heterogeneous microporosity. In this work, the second test sample of Estaillades carbonate rock has strong heterogenous microporosity. To consider the heterogeneity, the capillary pressure curve for each microporosity grid is given by the Leverett J-function:

$$J(s^w) = \frac{P_{ref}(s^w)}{\sigma_{ref}} \left(\frac{k_{ref}}{\varphi_{ref}} \right)^{1/2} = \frac{P_m^c(s^w)}{\sigma_m} \left(\frac{k_m}{\varphi_m} \right)^{1/2} \quad (9)$$

where the subscript ref and m denote the reference microporosity and the microporosity grid of interest, respectively. Combining Eqs. (2) and (9), the capillary pressure curve of the microporosity grid can be given by:

$$\begin{aligned} P_m^c(s^w) &= P_{ref}^c(s^w) \frac{\sigma_m}{\sigma_{ref}} \left(\frac{(r_{ref})^2 \varphi_{ref} \tau_m}{(r_m)^2 \varphi_m \tau_{ref}} \right)^{1/2} \left(\frac{\varphi_m}{\varphi_{ref}} \right)^{1/2} \\ &= P_{ref}^c(s^w) \frac{\sigma_m}{\sigma_{ref}} \left(\frac{r_{ref}}{r_m} \right) \left(\frac{\tau_m}{\tau_{ref}} \right)^{1/2} \end{aligned} \quad (10)$$

For the used samples in this work, we assume that microporosity has a constant tortuosity value. As a result, the capillary pressure curve depends exclusively on the entry-pressure radius, surface tension and contact angle values, and VG fitting parameters.

(2) Determining the percolation pressure P_{pe} . We define the capillary pressure at which the non-wetting phase breaks through microporosity grid as the percolation pressure. When the non-wetting phase pressure exceeds the percolation pressure of an invaded microporosity grid, the connected grids are allowed to be invaded by the non-wetting phase. This critical parameter can be related to the percolation saturation, s_{pe} , by:

$$P_{pe} = P_c(s_{pe}) \quad (11)$$

The percolation saturation can be obtained by the PNM in step (1). Uniform s_{pe} values are assigned to geometrically similar microporosity grids.

2.3.2. Main imbibition process

Once the non-wetting phase pressure or the wetting phase saturation reaches a preset value, the nonwetting phase pressure is decreased stepwise to perform the main imbibition process. For resolved pores, three pore-scale displacement mechanisms are considered, i.e., piston-like advance, snap-off, and cooperative filling (Valvatne, 2004; Chen et al., 2020). The capillary entry pressure for piston-like advance and the critical pressure for snap-off are calculated following (C.-Z. Qin and van Brummelen, 2019). For each pore body, the capillary entry pressure of the wetting phase is dynamically adjusted based on the number of connected throats and their invading conditions (Blunt, 1998):

$$P_{c,i} = \frac{2\sigma\cos\theta}{r + \sum_{i=1}^n C_i x_i r_i} \quad (12)$$

where r represents the inscribed radius of pore body, n denotes the number of connected throats filled by the wetting phase, i refers to a pore throat connected to the pore body and filled by wetting phase. For each pore throats, we assign C_i an arbitrary parameter, x_i a random number between 0 and 1, and r_i as its inscribed radius. The boundaries of microporous subdomains adjacent to a resolved pore, can be approximated as rough-walled boundaries. As demonstrated by Bultreys et al. (2016b), its influence on the interfacial curvature within macropores is negligible. Consequently, the Young-Laplace equation remains applicable for the pore bodies connected with microporosity grids.

The main imbibition starts at the end of the primary drainage, where the wetting phase is at irreducible saturation. The saturation at the start of main imbibition is a key factor to capillary hysteresis, as it dictates the shape of the imbibition capillary pressure curve and the final residual non-wetting phase saturation. This hysteretic effect also exerts a

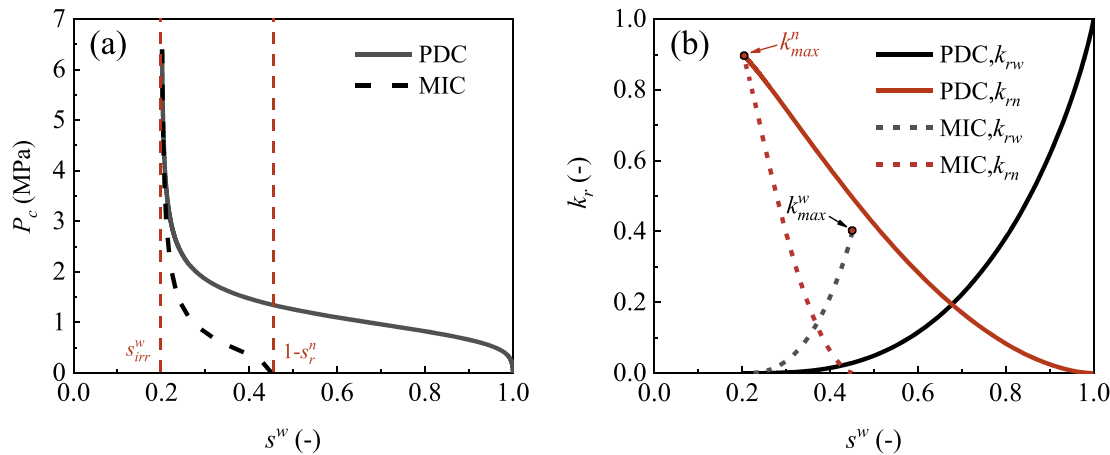


Fig. 5. Schematic of (a) the capillary pressure curves and (b) relative permeability curves for the primary drainage and the main imbibition processes.

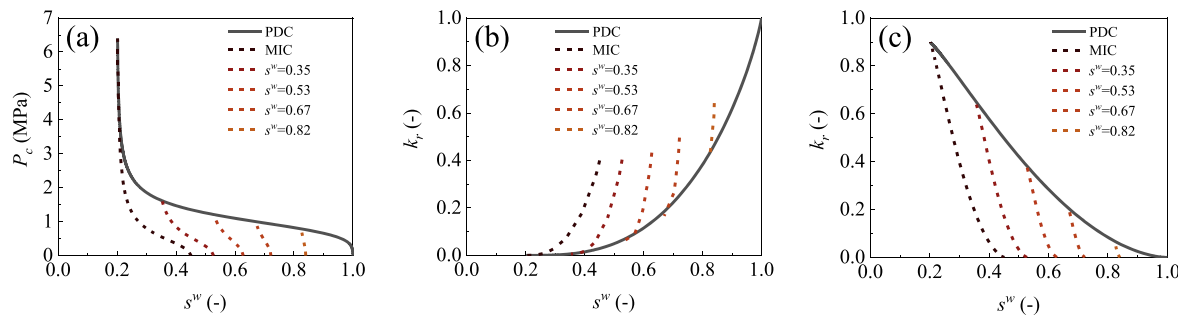


Fig. 6. (a) The capillary pressure curves during the main imbibition by Land model. (b) The wetting and (c) the non-wetting relative permeability curves during the main imbibition by the Killough model. The schematic diagram shows the results of the main imbibition at four different initial wetting saturations.

significant influence on relative permeability. Empirical observations reveal that higher initial non-wetting saturation at the end of the primary drainage correlates with enhanced non-wetting phase relative permeability and suppressed wetting phase relative permeability at the same saturation (Akbarabadi and Piri, 2013). The displacement mechanisms applied in the pore network of resolved pores can effectively capture this hysteresis phenomenon, as shown in Hefny et al. (2020). But, for microporosity grids, we employ the Land model and the Killough model to characterize capillary pressure hysteresis and relative permeability hysteresis, respectively.

To quantify the capillarity hysteresis, we first need to obtain the bounding drainage and imbibition curves, as shown in Fig. 5(a). The bounding drainage curve, known as the primary drainage curve (PDC), starts from a state where pore spaces are fully saturated with the wetting phase. The bounding imbibition curve, referred to as the main imbibition curve (MIC), initiates from the irreducible wetting-phase saturation. We describe the relationship between \$P_c\$ and \$s_e^w\$ using Eq. (5) after normalizing the wetting phase saturation. Note that the effective saturation of PDC is calculated using Eq. (8), while the effective saturation of MIC is correlated to the residual saturation:

$$s_e^w = \frac{s^w - s_{ir}^w}{1 - s_r^n - s_{ir}^w} \quad (13)$$

For microporosity grids with different initial saturation during the main imbibition process, we can replace \$s_r^n\$ and \$s_{ir}^w\$ in Eq. (13) with \$s_r^{n*}\$ and \$s_{ir}^{w*}\$, where \$s_{ir}^{w*}\$ represents the wetting phase saturation of microporosity grids at the beginning of main imbibition, and \$s_r^{n*}\$ can be predicted by the Land trapping model as follows:

$$s_r^{n*} = \frac{1 - s_{ir}^{w*}}{1 + C_L(1 - s_{ir}^{w*})} \quad (14)$$

where the coefficient \$C_L\$ is determined by (Land, 1968):

$$C_L = \frac{1}{s_r^n} - \frac{1}{1 - s_{ir}^w} \quad (15)$$

Taking into account the history-dependence of saturation, the capillary pressure curve for the main imbibition can be given by:

$$P_c^*(s^w) = P_c^{PDC}(s^w) - (P_c^{PDC}(s^w) - P_c^{MIC}(s^w)) \left(\frac{s^w - s_{ir}^{w*}}{1 - s_r^{n*} - s_{ir}^{w*}} \right)^a \quad (16)$$

where \$a\$ is the interpolation exponent for capillary pressure, the value of \$s^w\$ ranges between \$s_{ir}^{w*}\$ to \$1 - s_r^{n*}\$. The test results of the above hysteresis model under varying initial saturations are presented in Fig. 6(a).

We use Eqs. (6) and (7) to fit the relative permeability curves during the primary drainage and the main imbibition in Fig. 5(b), and then calculate hysteretic relative permeability in combination with the Killough model. The non-wetting phase relative permeability in the main imbibition is given as:

$$k_{r,n}^{MIC*}(s^n) = k_{r,n}^{PDC}(s_f^n) \left[\frac{k_{r,n}^{MIC}(s^n) - k_{r,n}^{MIC}(s_r^n)}{k_{r,n}^{MIC}(1 - s_{ir}^w) - k_{r,n}^{MIC}(s_r^n)} \right] \quad (17)$$

where \$k_{r,n}^{PDC}\$ and \$k_{r,n}^{MIC}\$ are the non-wetting phase relative permeability during the primary drainage and the main imbibition, respectively, \$s_f^n\$ is the non-wetting phase saturation at the beginning of the main imbibition which equals to \$1 - s_{ir}^{w*}\$. When calculating the hysteretic non-wetting phase permeability, \$S_f^n\$ should be normalized following Eq. (8), \$s_r^n\$ and \$1 - s_r^n\$ are normalized using Eq. (11), and \$s^n\$ under each capillary pressure is normalized by:

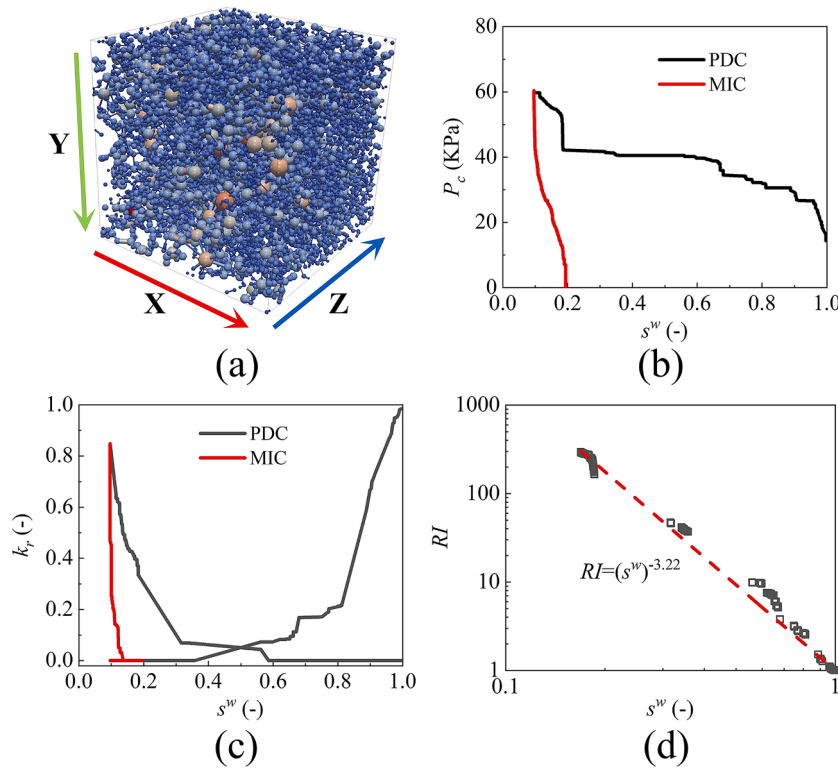


Fig. 7. (a) The extracted pore network for the RT1 subdomain. (b) Capillary pressure, (c) relative permeability, and (d) resistivity index curves for the RT1 subdomain.

$$s_{norm}^n = \left[\frac{(s^n - s_r^{n*})(1 - s_r^n - s_{ir}^w)}{s_f^n - s_r^{n*}} \right] + s_r^n \quad (18)$$

For the wetting phase relative permeability in the main imbibition, it can be calculated from:

$$k_{r,w}^{MIC*}(s^n) = k_{r,w}^{PDC}(s_f^n) + \left[\frac{k_{r,w}^{MIC}(s^n) - k_{r,w}^{MIC}(s_{ir}^w)}{k_{r,w}^{MIC}(s_r^n) - k_{r,w}^{MIC}(s_{ir}^w)} \right] \left[k_{r,w}^{MIC}(s_r^{n*}) - k_{r,w}^{PDC}(s_f^n) \right] \quad (19)$$

where $k_{r,w}^{MIC}(s_r^{n*})$ is the wetting phase relative permeability at the residual saturation s_r^{n*} and can be expressed as:

$$k_{r,w}^{MIC}(s_r^{n*}) = k_{r,w}^{PDC}(s_r^{n*}) + \Delta k_{r,w} \left(\frac{s_r^{n*}}{s_r^n} \right)^b \quad (20)$$

where b is the interpolation exponent for the wetting phase relative permeability, and $\Delta k_{r,w}$ is the relative permeability difference between the primary drainage and the main imbibition at the residual saturation s_r^n , formulated as:

$$\Delta k_{r,w} = k_{r,w}^{MIC}(s_r^n) - k_{r,w}^{PDC}(s_r^n) \quad (21)$$

To test the performance of the Killough hysteresis model, we plot the non-wetting phase relative permeability curves under various initial values of imbibition saturation in Fig. 6(b), while Fig. 6(c) shows the wetting relative permeability curves with $b = 0.5$.

2.3.3. Calculations of core-scale flow properties

For any given capillary pressure during the drainage or the imbibition, local saturation and conductivity of each phase can be determined by the quasi-static modeling. At a given saturation distribution across the sample, we calculate the steady-state flow of each phase using the following volumetric conservation equation for that phase in a pore body i or continuum grid cell i :

$$\sum_j Q_{ij} = 0 \quad \forall i \quad (22)$$

where

$$Q_{ij} = g_{ij}(P_i - P_j), \quad (23)$$

where j is the index for computational elements (pore body or continuum grid cell) connected to i , P is pressure, g_{ij} [$\text{m}^4/\text{Pa}/\text{s}$] is conductivity and correlates with the type of connected elements. The calculation details of hydraulic conductivity can be seen in Shi et al. (2024).

After obtaining the flow rate of each phase from pressure distribution for the whole sample, the phase permeability at a given saturation is calculated using the Darcy equation. The absolute permeability for single-phase flow is determined using the same method. Normalizing the phase permeability by the absolute permeability yields the relative permeability. Finally, complete relative permeability curves are generated by repeating this process across a series of saturation points during the drainage and imbibition. The resistivity index of sample as a function of wetting phase saturation can be obtained in a similar way. In the governing equations provided above, electrical conductivity (g) replaces hydraulic conductivity, electric current (Q) corresponds to flow rate, electrical potential (P) substitutes pressure, and finally, Ohm's law is used to calculate the resistivity index.

3. Result and discussion

3.1. ANLEC sandstone

To determine material and flow properties for microporosity grids, a subsample ($300 \times 300 \times 300$ voxels) was first extracted from the center of the RT1 subdomain (see Fig. 1). Then, we utilized a marker-based watershed segmentation (Gostick, 2017) to extract the pore network as shown in Fig. 7(a). The classic PNM (Hefny et al., 2020) was

Table 1

Summary of parameter values and formulas used for microporosity grids.

Flow process	PDC	MIC
α	2.67×10^{-5}	4.70×10^{-5}
Percolation saturation s_{pe}	0.6	
N	9.2	4.04
M	0.89	0.75
κ	2.29	-2.12
ς	7.54	5.47
Irreducible saturation s_{ir}^w	0.09	
Residual saturation s_r^n	0.81	
k_{max}^w	-	0.00054
k_{max}^n	0.85	
Permeability of microporosity k (m^2)	1.26×10^{-12}	
Average porosity of microporosity φ	0.17	
Formation factor (F)	60.15	
Resistivity index (RI)	$(s^w)^{-3.22}$	

performed to obtain the flow properties of RT1, including absolute permeability, the capillary pressure curve (Fig. 7(b)), the relative permeability curve (Fig. 7(c)), and the resistivity index curve (Fig. 7(d)). The interfacial tension and contact angle values of gas-mercury system were set to 0.48 N/m and 50°, respectively. The electrical conductivity of the wetting phase was set to 1 S/m, and flow was along the Z direction. Finally, the VG model and the Archie equation were utilized to fit the simulated results. The final values of input parameters for homogeneous microporosity are summarized in Table 1. We conduct quasi-static two-phase flow simulations by the developed PNCM. Moreover, a full-scale pore network was extracted from the image as shown in Fig. 1(b), and its numerical results are used as the reference to verify the PNCM model. The interfacial tension, contact angle, electrical conductivity, and flow direction for two case studies of the whole rock sample are the same as those of the representative PNM of microporosity.

The values of absolute permeability and formation factor, which are the key parameters characterizing single-phase flow, calculated by the PNCM are 1.92 D and 62.4, respectively. These results are in good agreement with the values 2.17 D and 52.4 by the reference (i.e., by the full-scale PNM). Moreover, good agreement between the PNCM and the full-scale PNM is observed in Fig. 8 for both capillary pressure and relative permeability curves in both drainage and imbibition processes. In the drainage, an obvious "permeability jail", in which both wetting and non-wetting phases exhibit extremely low permeability at a wide range of saturation values (Cluff and Byrnes, 2010), is caused by the layered pore structures. Snap-off and trapping events are easily triggered in such layered pore structures, resulting in significant residual non-wetting phase within pores at the end of imbibition.

For the saturation and resistivity relationship in the drainage, both full-scale PNM and PNCM predict the non-Archie electrical behavior (see Fig. 9) caused by multiscale layered pore structures. At high wetting-phase saturations (>0.5), the dominant percolation pathway composed of resolved pores is first invaded by the non-wetting phase,

which triggers a sharp rise in the resistivity index curve. When the wetting-phase saturation decreases below 0.5, the non-wetting phase starts to invade smaller pores in the RT1. Meanwhile, the main percolation pathway is formed by the remaining wetting films at pore corners, which results in the increasing trend of the resistivity index curve slowing down. To sum up, the developed PNCM together with well-characterized flow properties of microporosity can accurately predict both single-phase and two-phase flow properties of multiscale rock samples with homogeneous microporosity.

3.2. Estaillades carbonate

For Estaillades carbonate with heterogeneous microporosity, proper estimation of porosity and entry-pressure radius for each microporosity grid is essential (Shan Wang et al., 2022). Porosity was determined by mathematically averaging the values of mapped voxels in the porosity map (c.f., Fig. 2(c)). For the entry-pressure radius, instead of characterizing it via in-situ CT scanning and the image difference technique, we developed a simple stochastic sampling approach based on the dual-pore-size distribution obtained from MICP. Since part of macropores cannot be resolved at the current image resolution, microporosity grids are categorized into two types, i.e., MT1 and MT2. MT1 represents high-porosity microporosity grids containing unresolved macropores, while MT2 represents low-porosity microporosity grids containing unresolved micropores. Finally, the entry radii for MT1 and MT2 were assigned based on their respective PSDs. The details of the workflow are provided in Appendix A.

Although the capillary pressure curves for macropores and micropores in the Estaillades carbonate rock can be parameterized using the MICP data and the bimodal VG model, modeling relative permeability

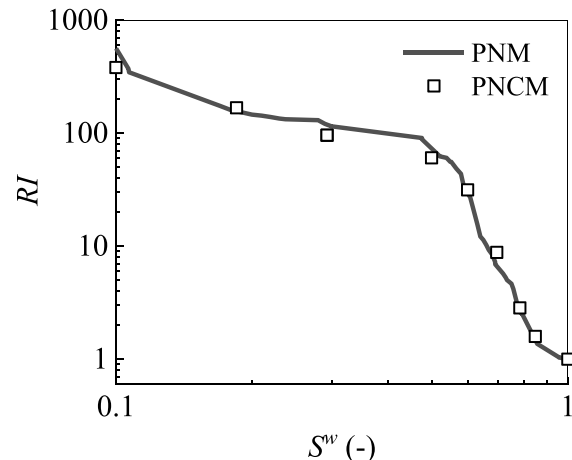


Fig. 9. The comparison of drainage resistivity index curve predicted by the PNCM and the full-scale PNM.

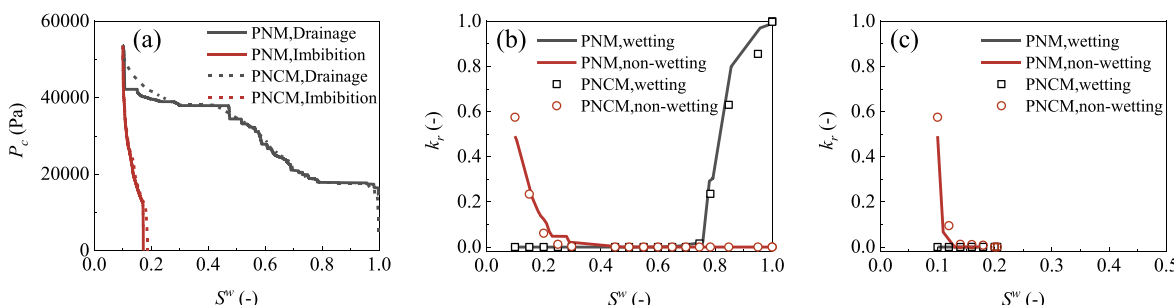


Fig. 8. ANLEC sandstone (a) capillary pressure curves, (b) relative permeability curves in the drainage, and (c) relative permeability curves in the imbibition, predicted by the full-scale PNM and the PNCM.

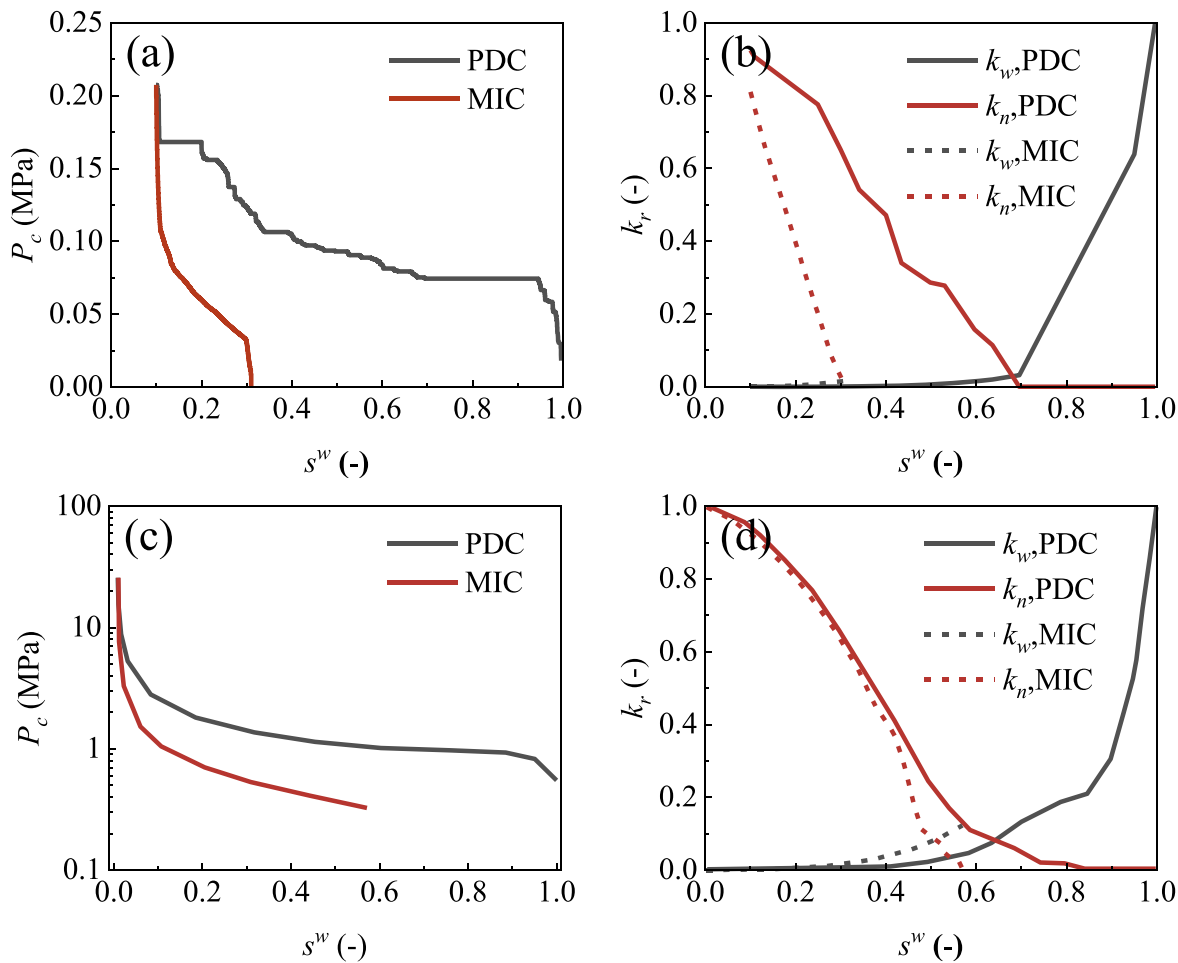


Fig. 10. Capillary pressure curve and relative permeability curve for microporosity grids. (a) and (b) were obtained via PNM simulations in resolved pores and correspond to MT1. (c) And (d) are adapted from (Bultreys et al., 2016a) and correspond to MT2.

Table 2
Summary of the input parameters for MT1 and MT2.

Microporosity type	MT1	MT2	
Flow process	PDC	MIC	PDC
Entry pressure P_e	r	$1.66r$	r
	$\frac{2\sigma\cos\theta}{2\sigma\cos\theta}$	$\frac{2\sigma\cos\theta}{2\sigma\cos\theta}$	$\frac{2\sigma\cos\theta}{2\sigma\cos\theta}$
Percolation saturation s_{pe}	0.7		
N	4.20	4.72	5.80
M	$1 - 1/N$		2.68
κ	4.67	-1.09	6.32
ζ	0.67	0.22	0.37
Irreducible saturation s_{ir}^w	0.02		0.01
Residual saturation s_r^n	0.69		0.43
k_{max}^w	-	0.02	-
k_{max}^n	0.99		0.99
Permeability of microporosity k (m^2)	$\varphi r^2 / 32\tau^2$		
Average porosity of microporosity φ		Image difference technology	
Tortuosity τ	1.75		
Formation factor (F)	φ^{-2}	-	φ^{-2}
Resistivity index (RI)	$(s^w)^{-2}$	-	$(s^w)^{-2}$

curves still requires additional raw data or parameters. Thus, representative pore network simulations for microporosity remain indispensable. Fig. 10 shows the capillary pressure and relative permeability curves for MT1 and MT2 grids. The representative pore network for MT1 grids was extracted from the resolved pores in Fig 2(b). For the MT2 grids, the curves were adapted from (Bultreys et al., 2016a), which were derived from PNM simulations on a generated unstructured network exhibiting a PSD similar to that of MICP results. It is seen that the

Table 3
Summary of measured and simulated single-phase transport properties for the Estaiades carbonate rock.

Transport property	φ (%)	k (mD)	F
Experimental ^a	25	273 ± 16	24 ± 0.24
Classical PNM	10.6	126.62	126.47
PNCM	25.5	275.81	15.10

^a from Bauer et al. (2012).

capillary pressure curves and relative permeability curves in the primary drainage exhibit a similar trend for both MT1 and MT2. However, in the main imbibition, the residual non-wetting saturation for MT1 is much higher than that of MT2, due to the strong heterogeneity and poor connectivity of resolved pores.

Eqs. (5–7) were employed to determine the input parameters for the PNCM. Regarding the electrical characteristics of microporosity grids, we utilized the same parameters as in Bultreys et al. (2015). The formation factor for each grid was calculated using $F = \varphi^{-2}$, while the resistivity of unsaturated grids was determined by the Archie's second equation as $RI = S_w^{-2}$. In summary, the input parameters for the two types of microporosity grids are detailed in Table 2. Quasi-static water-decane flow in the Estaiades carbonate rock is simulated by the PNCM. The interface tension is 48.3 mN/m and the uniform contact angle is 0°. Flow is along the X direction. A constant tortuosity value of 1.75 is assigned to all microporosity grids.

Table 3 shows the single-phase transport properties by experiments,

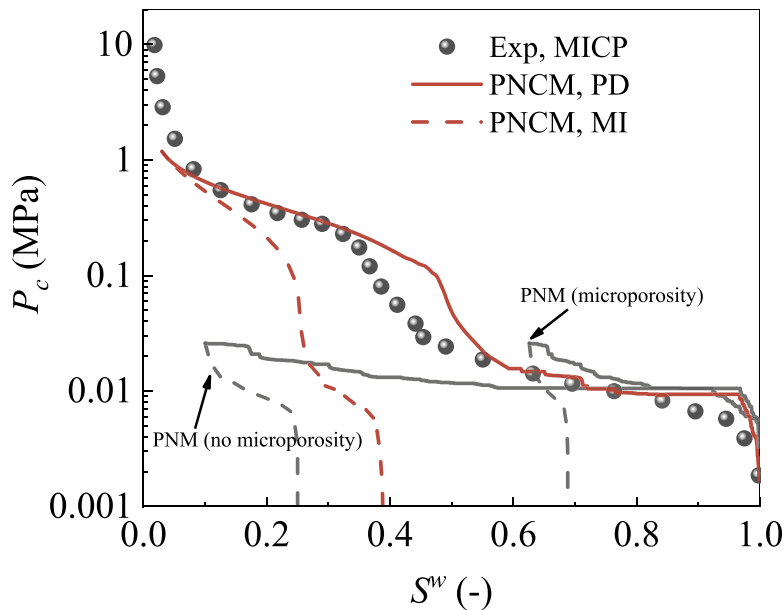


Fig. 11. The capillary pressure curves by the PNCM and the classical PNM, compared with the MICP data from Bultreys et al. (2015). The MICP curve was rescaled to the water-decane system using interfacial tension (48.3 mN/m) and contact angle (0°). PNM with microporosity and no microporosity represent the saturation of wetting phase normalized by total porosity and resolved pores, respectively.

PNM of resolved pores and the PNCM. It is seen that the PNM underestimates the absolute permeability, and overestimates the formation factor. This discrepancy is primarily attributed to the neglect of sub-resolution pores, which serve as bridges among resolved pores, and significantly influence the permeability prediction. After characterizing the properties of microporosity, the absolute permeability predicted by the PNCM is in consistence with the experimental values. Our findings differ from those in Bultreys et al. (2015), which showed that micro-porosity in Estaillades had negligible impact on the absolute permeability. The reason may be that uniform flow properties were applied to all Darcy-type micro-links in their model. Regarding the formation factor, the value predicted by the PNCM is lower than the measured value of 24 ± 0.24 as shown in Table 3. This may be caused by underestimating the electrical cementation coefficient of microporosity, sample heterogeneity, or the smaller size of the simulated domain than that of the measured rock sample. If adjusting the electrical cementation coefficient of microporosity to 2.5, it yielded a formation factor of 20.5, which is much closer to the measured value.

Fig. 11 shows the comparison of the drainage capillary pressure

curves predicted by the models of both PNM of resolved pores and PNCM with the MICP data. The capillary pressure values were rescaled to represent the water-decane system. It is seen that the capillary pressure curve predicted by the PNCM is in agreement with the experimental one, with a slight deviation in the range of 2×10^4 to 2×10^5 Pa. The observed deviation can be attributed to the ink-bottle effect during the mercury intrusion process (Moro and Böhni, 2002), causing underestimation of large pore-throat volumes and subsequent alteration of entry pressures of microporosity grids. This conclusion is verified by the test cases with a larger ratio of MT1 to MT2 (see Appendix B). Moreover, the capillary pressure curve by the PNM deviates from the experimental trend because it neglects microporosity, which accounts for 60 % of the total porosity. After rescaling the saturation by the measured total porosity, the PNM result is close to the mercury intrusion curve in the high-saturation region. Unlike the relatively flat curve of the MIC by the PNM of resolved pores, the results by the PNCM reveal twice distinct rapid saturation changes, corresponding to the sequential invasion of the wetting phase into microporosity and resolved pores.

Fig. 12(a) compares the measured and simulated relative

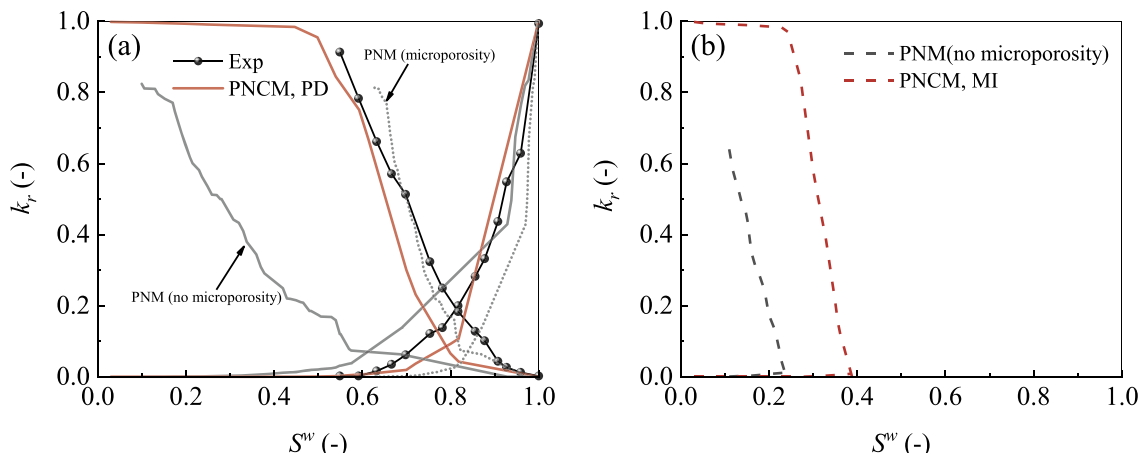


Fig. 12. (a) Measured and simulated drainage relative permeability curves for the Estaillades carbonate rock. (b) Simulated imbibition relative permeability curves for the main imbibition. The reference relative permeability curves for drainage are adopted from Ott et al. (2015).

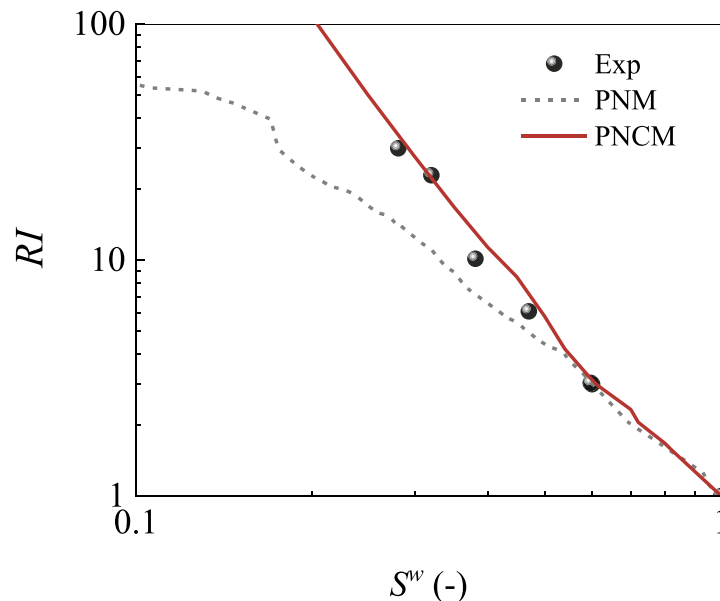


Fig. 13. Drainage resistivity index curve from PNCM and classical PNM, compared to the experimental results estimated from the graph published in Han et al. (2007).

permeability curves in the drainage process. It is seen that the PNCM results match well with the water-decane relative permeability from experimental measure. It is seen that the invaded pore spaces with the wetting saturation from 1 to 0.6 contribute to 80 % of the non-wetting permeability, indicating the presence of well-connected macropores. Additionally, the experimental data is in close agreement with the PNM results rescaled by the measured total porosity, indicating that microporosity with well-connected macropores mainly impacts the normalized saturation. For the imbibition process, we do not have experimental data to verify the PNCM. However, the imbibition curve by the PNCM in Fig. 12(b) shows a similar trend to the results obtained by the DPNM in Bultreys et al. (2016a). At the beginning, the wetting phase invades small pores in microporosity, where saturation changes negligibly affect the non-wetting permeability. As the wetting phase invades macropores, the heterogeneous pore structures trigger non-wetting phase trapping and snap-off, causing a sharp decline in its relative permeability. At the end of imbibition, a large amount of the non-wetting phase remains trapped within multiscale pore spaces, resulting in low relative permeability for both phases.

Fig. 13 compares the resistivity index curves obtained from experimental measurements, the PNM of resolved pores and the PNCM. In contrast to the curve by the PNM, the PNCM results exhibit close agreement with the experimental data. Compared to the DPNM incorporating Darcy-type pores or micro-links (Bauer et al., 2011; Bultreys et al., 2015), the PNCM achieves superior prediction accuracy with less dependence on parameter fine-tuning.

4. Conclusions

In this work, we have extended our numerical framework of pore-network-continuum modeling to quasi-static two-phase flow in multi-scale digital rocks. In the model development, we employ two basic parameters (i.e., porosity and entry-pressure radius) and classic empirical equations including the Katz-Thompson model, the van Genuchten model, the Archie equation, the Land model, the Killough model, and the Leverett J-function, to characterize flow properties of heterogeneous microporosity. Moreover, we propose a MICP-based stochastic sampling approach to assign entry-pressure radii to microporosity grids. The developed model is then applied to a laminated sandstone with synthesized homogeneous microporosity and an Estaillades carbonate rock

with heterogeneous microporosity, to predict their flow properties including absolute permeability, formation factor, resistivity index, capillary pressure, and relative permeability. Based on a number of case studies, we draw the following main conclusions:

- (1) For the laminated sandstone with homogeneous microporosity, compared with numerical predictions by the full-scale pore-network modeling (i.e., the verification data), the developed pore-network-continuum model can well predict the single-phase flow properties of absolute permeability and formation factor, and the two-phase flow properties of resistivity index, capillary pressure, and relative permeability for both primary drainage and main imbibition.
- (2) For the carbonate rock with realistic heterogeneous microporosity, with the proposed low-cost characterization approach for microporosity properties, the developed pore-network-continuum model can adequately predict the single-phase flow properties of absolute permeability and formation factor, and the two-phase flow properties of resistivity index, capillary pressure, and relative permeability for the primary drainage, compared with experimental data.
- (3) The “permeability jail” in the primary drainage for the laminated sandstone is observed. For the carbonate rock, step-wise increase and decrease of capillary pressure in the primary drainage and main imbibition are predicted, and the relative permeability curves for the main imbibition dramatically shift to the left due to the severe trapping of non-wetting phase in multiscale pore structures.

While the developed quasi-static two-phase pore-network-continuum model performs well, we comment on a few some uncertainties that may affect its numerical predictions. First, for Estaillades carbonate rock, it is challenging to construct representative pore structures of highly heterogenous microporosity. As an alternative, we adopted flow properties of a numerically generated pore network based on the pore-size distribution of microporosity from MICP. Second, in-situ CT images show that the distribution of pore sizes of microporous domain of Estaillades carbonate rock appears to be spatially correlated, which has not been considered in our current stochastic sampling approach.

Data availability

The datasets of Estaillades Carbonate sample were obtained through the Digital Rock Portal (<https://www.digitalrockspotal.org>). Other data will be made available upon request (chaozhong.qin@gmail.com).

CRediT authorship contribution statement

Bowen Shi: Writing – original draft, Validation, Software, Formal analysis. **Jianqi Rong:** Investigation, Formal analysis. **Han Jiang:** Writing – original draft, Validation, Software, Investigation. **Bo Guo:** Methodology, Conceptualization. **S. Majid Hassanizadeh:** Writing – review & editing, Supervision. **Chao-Zhong Qin:** Writing – review &

Appendix A

The workflow for determining the heterogeneous entry radii for microporosity grids

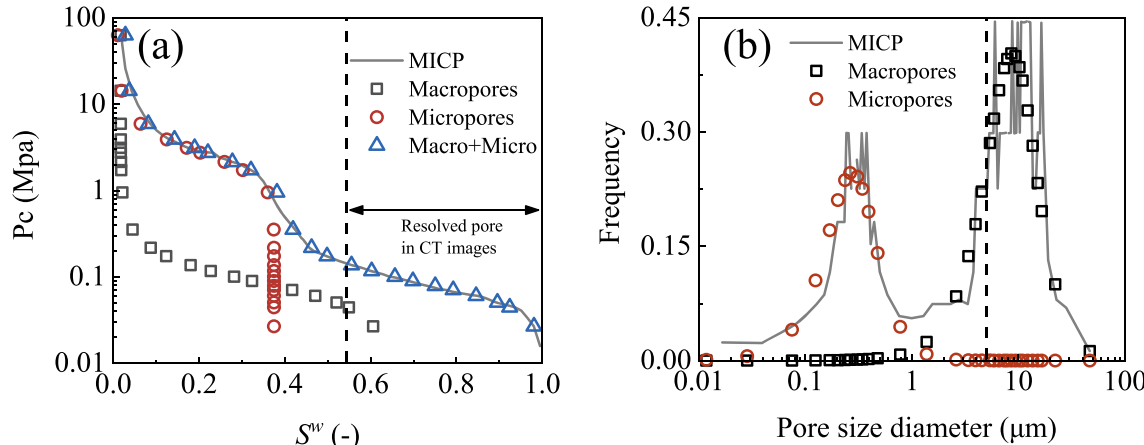


Fig. A1. (a) The mercury intrusion curves, and (b) the pore-size distribution of the Estaillades carbonate rock. The black and red points are the fitted macropore and micropore distributions using the bimodal van Genuchten model. The black dashed line represents the proportion of resolved pores obtained from the segmented CT images, which was used to determine the threshold pore sizes for distinguishable resolved pores and microporosity.

Fig. A1(a) shows the \$P_c(S^w)\$ curve from an MICP experiment. It is seen that the Estaillades carbonate with multiscale pore structures exhibits rapid saturation declines in the ranges of 1~10 MPa and 0.03~0.2 MPa, indicating mercury intrusion into macropores and micropores, respectively. To quantify the proportions of macropores and micropores, the bimodal van Genuchten model was used to decompose the \$P_c(S^w)\$ curve (Durner, 1994):

$$S_e^w = \sum_{i=1}^2 w_i [1 + (\alpha_i P_c)^{N_i}]^{-M_i} \quad (\text{A1})$$

where \$S_e^w\$ is the effective saturation of wetting phase, \$P_c\$ is the invasion pressure, \$w_i\$ (\$i = 1, 2\$) are the volumetric fractions of macropore and micropore phases, respectively, \$N_i\$ are the fitted dimensionless parameters, and \$M_i\$ is determined in terms of \$N_i\$ (i.e., \$M_i = 1 - 1/N_i\$). The black squares and red circles in Fig. A1(a) respectively depict separate intrusion curves for macropores (\$w_1 = 62\%\$) and micropores (\$w_2 = 38\%\$). By multiplying the fitted volumetric fractions with the measured total porosity, we can obtain the porosities for macropores and micropores as 0.16 and 0.12, respectively. It is worth noting that the order of mercury intrusion into pore spaces is correlated to the connection between pores and throats, which means the estimated macropore porosity according to the \$P_c(S^w)\$ curve and the bimodal van Genuchten model may be lower than the actual value.

The capillary pressure of the measured MICP curve was transformed into pore sizes by the Young-Laplace equation with the interfacial tension of 0.483 N/m and the contact angle of 40° for mercury. Then, the probability distribution function was used to calculate the pore-size distributions (PSDs):

$$f(r) = r \frac{dS_w}{dr} \quad (\text{A2})$$

Fig. A1(b) shows the macropore and micropore PSDs derived from MICP analysis. Unlike previous studies that used voxel size (3.1 \$\mu\text{m}\$) as the threshold to distinguish the PSD between resolved pores and unresolved pores (i.e., microporosity), we determined the threshold radius based on the volume fraction of resolved pores obtained from the image processing. As indicated by the dashed line in Fig. A1(a), we first acquired the capillary pressure at which the resolved pores are fully invaded, and then calculated the threshold radius (dashed line in Fig. A1(b)) using the Young-Laplace equation. It is found that part of macropores could not be reconstructed. Therefore, we categorized microporosity grids into two types, namely, MT1 and MT2. MT1 represents high-porosity microporosity grids containing unresolved macropores, while MT2 represents low-porosity microporosity grids containing unresolved micropores.

We first ranked all microporosity grids by descending porosity values. Then, the top-ranked voxels were sequentially labeled as MT1 until

cumulative porosity (combined with resolved macropores) reached the estimated macropore porosity of 0.16. Finally, due to a weak correlation between voxel porosity and entry pressure (Shan Wang et al., 2022), the entry radii for MT1 and MT2 grids were stochastically assigned based on their respective PSDs shown in Fig. A1(b), with all sampled values constrained below the threshold values.

Appendix B

Test cases for Estaillades carbonate with adjusted volume fraction of macropores in microporosity

We conducted case studies of the Estaillades carbonate rock with three different volume fractions of macropores in microporosity. The value of 0.62 derived from the MICP curve (c.f., Appendix A) and two manually adjusted values, 0.7 and 0.8, were employed.

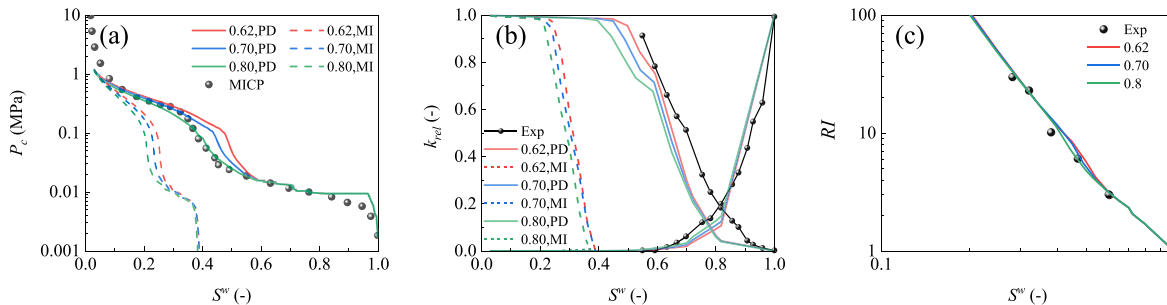


Fig. B1. (a) The capillary pressure curves, (b) relative permeability curves and (c) resistivity index curves predicted by the PNCM, under three different volume fractions of macropores in microporosity.

Fig. B1 shows the capillary pressure curves, relative permeability and resistivity index curves by the PNCM under three different volume fractions of macropores in microporosity. It is seen that the capillary pressure curve predicted by the PNCM with a value of 0.80 matches the experimental curve best. But for relative permeability curves and resistivity index curves, the influence is negligible.

References

- Aghaei, A., Piri, M., 2015. Direct pore-to-core up-scaling of displacement processes: dynamic pore network modeling and experimentation. *J. Hydrol.* 522, 488–509. <https://doi.org/10.1016/j.jhydrol.2015.01.004>.
- Akbarabadi, M., Piri, M., 2013. Relative permeability hysteresis and capillary trapping characteristics of supercritical CO₂/brine systems: an experimental study at reservoir conditions. *Adv. Water. Resour.* 52, 190–206. <https://doi.org/10.1016/j.advwatres.2012.06.014>.
- Archie, G.E., 1942. The electrical resistivity log as an aid in determining some reservoir characteristics. *Trans. AIME* 146 (01), 54–62. <https://doi.org/10.2118/942054-G>.
- Bauer, D., Youssef, S., Fleury, M., Bekri, S., Rosenberg, E., Vizika, O., 2012. Improving the estimations of petrophysical transport behavior of carbonate rocks using a dual pore network approach combined with computed microtomography. *Transp. Porous. Media* 94 (2), 505–524. <https://doi.org/10.1007/s11242-012-9941-z>.
- Archie, G.E., 1942. The electrical resistivity log as an aid in determining some reservoir characteristics. *Trans. AIME* 146 (01), 54–62. <https://doi.org/10.2118/942054-G>.
- Bauer, D., Youssef, S., Han, M., Bekri, S., Rosenberg, E., Fleury, M., Vizika, O., 2011. From computed microtomography images to resistivity index calculations of heterogeneous carbonates using a dual-porosity pore-network approach: influence of percolation on the electrical transport properties. *Phys. Rev. Stat. Nonlin. Softw. Matter. Phys.* 84 (1 Pt 1), 011133. <https://doi.org/10.1103/PhysRevE.84.011133>.
- Bijeljic, B., Mostaghimi, P., Blunt, M.J., 2013. Insights into non-Fickian solute transport in carbonates. *Water. Resour. Res.* 49 (5), 2714–2728. <https://doi.org/10.1002/wr.20238>.
- Blunt, M.J., 1998. Physically-based network modeling of multiphase flow in intermediate-wet porous media. *J. Pet. Sci. Eng.* 20 (3), 117–125. [https://doi.org/10.1016/S0920-4105\(98\)00010-2](https://doi.org/10.1016/S0920-4105(98)00010-2).
- Blunt, M.J., Bijeljic, B., Dong, H., Gharbi, O., Iglauer, S., Mostaghimi, P., Pentland, C., 2013. Pore-scale imaging and modelling. *Adv. Water. Resour.* 51, 197–216. <https://doi.org/10.1016/j.advwatres.2012.03.003>.
- Brusseau, M.L., Guo, B., Huang, D., Yan, N., Lyu, Y.J.W.R., 2021. Ideal versus nonideal transport of PFAS in unsaturated porous media. *Water. Res.* 202, 117405.
- Bultreys, T., Stappen, J.V., Kock, T.D., Boever, W.D., Boone, M.A., Hoorebeke, L.V., Cnudde, V., 2016a. Investigating the relative permeability behavior of microporosity-rich carbonates and tight sandstones with multiscale pore network models. *J. Geophys. Res.: Solid Earth* 121 (11), 7929–7945. <https://doi.org/10.1002/2016jb013328>.
- Bultreys, T., Van Hoorebeke, L., Cnudde, V., 2015. Multi-scale, micro-computed tomography-based pore network models to simulate drainage in heterogeneous rocks. *Adv. Water. Resour.* 78, 36–49. <https://doi.org/10.1016/j.advwatres.2015.02.003>.
- Bultreys, T., Van Hoorebeke, L., Cnudde, V., 2016b. Simulating secondary waterflooding in heterogeneous rocks with variable wettability using an image-based, multiscale pore network model. *Water. Resour. Res.* 52 (9), 6833–6850. <https://doi.org/10.1002/2016wr018950>.
- Carrillo, F.J., Bourg, I.C., Soulaine, C., 2020. Multiphase flow modeling in multiscale porous media: an open-source micro-continuum approach. *J. Comput. Phys.* X 8. <https://doi.org/10.1016/j.jcpnx.2020.100073>.
- Carrillo, F.J., Soulaine, C., Bourg, I.C., 2022. The impact of sub-resolution porosity on numerical simulations of multiphase flow. *Adv. Water. Resour.* 161. <https://doi.org/10.1016/j.advwatres.2021.104094>.
- Chen, S., Qin, C., Guo, B., 2020. Fully implicit dynamic pore-network modeling of two-phase flow and phase change in porous Media. *Water. Resour. Res.* 56 (11). <https://doi.org/10.1029/2020wr028510>.
- Cluff, R.M., & Byrnes, A.P., 2010. *Relative permeability in tight gas sandstone reservoirs—the “Permeability Jail” model*. Paper presented at the SPWLA Annual Logging Symposium.
- Dai, J., Li, L., Lei, S., Yuting, J., Yukun, C., Shenghao, W., Chaozhong, Q., 2023. Limiting pathways and breakthrough pressure for CO₂ flow in mudstones. *J. Hydrol.* 625. <https://doi.org/10.1016/j.jhydrol.2023.129998>.
- Dong, H., Blunt, M.J., 2009. Pore-network extraction from micro-computerized-tomography images. *Phys. Rev. Stat. Nonlin. Soft. Matter. Phys.* 80 (3 Pt 2), 036307. <https://doi.org/10.1103/PhysRevE.80.036307>.
- Durner, W., 1994. Hydraulic conductivity estimation for soils with heterogeneous pore structure. *Water. Resour. Res.* 30 (2), 211–223.
- Feldmann, F., Hagemann, B., Ganzer, L., Panfilov, M., 2016. Numerical simulation of hydrodynamic and gas mixing processes in underground hydrogen storages. *Environ. Earth Sci.* 75 (16). <https://doi.org/10.1007/s12665-016-5948-z>.
- Foroughi, S., Bijeljic, B., Gao, Y., Blunt, M.J., 2024. Incorporation of sub-resolution porosity into two-phase flow models with a multiscale pore network for complex microporous rocks. *Water. Resour. Res.* 60 (4). <https://doi.org/10.1029/2023wr036393>.
- Fu, J., Thomas, H.R., Li, C., 2021. Tortuosity of porous media: image analysis and physical simulation. *Earth-Sci. Rev.* 212. <https://doi.org/10.1016/j.earscirev.2020.103439>.
- Gostick, J.T., 2017. Versatile and efficient pore network extraction method using marker-based watershed segmentation. *Phys. Rev. E* 96 (2–1), 023307. <https://doi.org/10.1103/PhysRevE.96.023307>.
- Han, M., Fleury, M., Levitz, P., 2007. Effect of the pore structure on resistivity index curves. In: Paper presented at the International Symposium of The Society of Core Analysts.
- Hefny, M., Qin, C., Saar, M.O., Ebigbo, A., 2020. Synchrotron-based pore-network modeling of two-phase flow in Nubian Sandstone and implications for capillary trapping of carbon dioxide. *Int. J. Greenh. Gas Control* 103. <https://doi.org/10.1016/j.ijggc.2020.103164>.
- Idowu, N.A., Blunt, M.J., 2009. Pore-scale modelling of rate effects in waterflooding. *Transp. Porous. Media* 83 (1), 151–169. <https://doi.org/10.1007/s11242-009-9468-0>.
- Jiang, H., Arns, C.H., 2020. A pore-scale upscaling approach for laminated sandstones using Minkowski maps and hydraulic attributes. *Water. Resour. Res.* 56 (8). <https://doi.org/10.1029/2020wr027978>.
- Jiang, H., Arns, C.H., 2021. Pore-scale MultiResolution rock-typing of layered sandstones via Minkowski Maps. *Water. Resour. Res.* 57 (4). <https://doi.org/10.1029/2020wr029144>.
- Jiang, Z., van Dijke, M.I.J., Sorbie, K.S., Couples, G.D., 2013. Representation of multiscale heterogeneity via multiscale pore networks. *Water. Resour. Res.* 49 (9), 5437–5449. <https://doi.org/10.1002/wrcr.20304>.

- Katz, A.J., Thompson, A.H., 1986. Quantitative prediction of permeability in porous rock. *Phys. Rev. B Condens. Matter.* 34 (11), 8179–8181. <https://doi.org/10.1103/physrevb.34.8179>.
- Katz, A.J., Thompson, A.H., 1987. Prediction of rock electrical-conductivity from mercury injection measurements. *J. Geophys. Res-Solid Earth Planets* 92 (B1), 599–607. <https://doi.org/10.1029/JB092iB01p00599>.
- Killough, J..J.S.o.P.E.J., 1976. Reservoir simulation with history-dependent saturation functions. *Soc. Pet. Eng. J.* 16 (01), 37–48.
- Land, C.S.J.S.O.P.E.J., 1968. Calculation of imbibition relative permeability for two-and three-phase flow from rock properties. *Soc. Pet. Eng. J.* 8 (02), 149–156.
- Liu, X., Wang, J., Ge, L., Hu, F., Li, C., Li, X., Xue, Q., 2017. Pore-scale characterization of tight sandstone in Yanchang Formation Ordos Basin China using micro-CT and SEM imaging from nm- to cm-scale. *Fuel* 209, 254–264. <https://doi.org/10.1016/j.fuel.2017.07.068>.
- Mason, G., Morrow, N.R., 1991. Capillary behavior of a perfectly wetting liquid in irregular triangular tubes. *J. Colloid. Interface Sci.* 141 (1), 262–274. [https://doi.org/10.1016/0021-9797\(91\)90321-X](https://doi.org/10.1016/0021-9797(91)90321-X).
- Mehmami, A., Prodanović, M., 2014. The effect of microporosity on transport properties in porous media. *Adv. Water. Resour.* 63, 104–119. <https://doi.org/10.1016/j.advwatres.2013.10.009>.
- Morel, D., Nectoux, A., Danquigny, J., 1997. Experimental determination of the mobility of hydrocarbon liquids during gas condensate reservoir depletion: three actual cases. In: Paper presented at the SPE Annual Technical Conference and Exhibition?.
- Moro, F., Böhni, H., 2002. Ink-bottle effect in mercury intrusion porosimetry of cement-based materials. *J. Colloid. Interface Sci.* 246 (1), 135–149. <https://doi.org/10.1006/jcis.2001.7962>.
- Niblett, D., Mularczyk, A., Niasar, V., Eller, J., Holmes, S., 2020. Two-phase flow dynamics in a gas diffusion layer - gas channel - microporous layer system. *J. Power. Sources*. 471. <https://doi.org/10.1016/j.jpowsour.2020.228427>.
- Ott, H., Pentland, C.H., Oedai, S., 2015. CO₂ – brine displacement in heterogeneous carbonates. *Int. J. Greenh. Gas Control* 33, 135–144. <https://doi.org/10.1016/j.ijggc.2014.12.004>.
- Pak, T., Butler, I.B., Geiger, S., van Dijke, M.I.J., Jiang, Z., Surmas, R., 2016. Multiscale pore-network representation of heterogeneous carbonate rocks. *Water. Resour. Res.* 52 (7), 5433–5441. <https://doi.org/10.1002/2016wr018719>.
- Patzek, T.W., 2001. Verification of a complete pore network simulator of drainage and imbibition. *SPE J.* 6 (02), 144–156. <https://doi.org/10.2118/71310-PA>.
- Piller, M., Schema, G., Nolich, M., Favretto, S., Radaelli, F., Rossi, E., 2009. Analysis of hydraulic permeability in porous Media: from high resolution X-ray tomography to direct numerical simulation. *Transp. Porous. Media* 80 (1), 57–78. <https://doi.org/10.1007/s11242-009-9338-9>.
- Prodanović, M., Mehmami, A., Sheppard, A.P., 2014. Imaged-based multiscale network modelling of microporosity in carbonates. *Geol. Soc. Lond. Spec. Publ.* 406 (1), 95–113. <https://doi.org/10.1144/sp406.9>.
- Qin, C.-Z., van Brummelen, H., 2019. A dynamic pore-network model for spontaneous imbibition in porous media. *Adv. Water. Resour.* 133. <https://doi.org/10.1016/j.advwatres.2019.103420>.
- Qin, C.Z., Wang, X., Hefny, M., Zhao, J., Chen, S., Guo, B., 2022. Wetting dynamics of spontaneous imbibition in porous Media: from pore scale to Darcy scale. *Geophys. Res. Lett.* 49 (4). <https://doi.org/10.1029/2021gl097269>.
- Ruspiñi, L.C., Ören, P.E., Berg, S., Masalmeh, S., Bultreys, T., Taberner, C., Wilson, O.B., 2021. Multiscale digital rock analysis for Complex rocks. *Transp. Porous. Media* 139 (2), 301–325. <https://doi.org/10.1007/s11242-021-01667-2>.
- Sadeghejad, S., Enzmann, F., Kersten, M., 2021. Digital rock physics, chemistry, and biology: challenges and prospects of pore-scale modelling approach. *Appl. Geochem.* 131. <https://doi.org/10.1016/j.apgeochem.2021.105028>.
- Saxena, N., Hofmann, R., Alpak, F.O., Berg, S., Dietderich, J., Agarwal, U., Wilson, O.B., 2017. References and benchmarks for pore-scale flow simulated using micro-CT images of porous media and digital rocks. *Adv. Water. Resour.* 109, 211–235. <https://doi.org/10.1016/j.advwatres.2017.09.007>.
- Shi, B., Jiang, H., Guo, B., Tian, J., Qin, C.-Z., 2024. Modeling of flow and transport in multiscale digital rocks aided by grid coarsening of microporous domains. *J. Hydrol.* 633. <https://doi.org/10.1016/j.jhydrol.2024.131003>.
- Soulaine, C., Gjetvaj, F., Garing, C., Roman, S., Russian, A., Gouze, P., Tchelapi, H.A., 2016. The impact of sub-resolution porosity of X-ray microtomography images on the permeability. *Transp. Porous. Media* 113 (1), 227–243. <https://doi.org/10.1007/s11242-016-0690-2>.
- Sun, Z., Torres-Verdin, C., 2022. The role of pore-shape and pore-space heterogeneity in Non-Archie Behavior of resistivity index curves. *J Geophys Res: Solid Earth* 127 (9). <https://doi.org/10.1029/2022jb024792>.
- Valvatne, P.H. (2004). *Predictive pore-scale modelling of multiphase flow*.
- van Genuchten, M.T., 1980. A closed-form equation for predicting the hydraulic conductivity of unsaturated soils. *Soil. Sci. Soc. Am. J.* 44 (5), 892–898. <https://doi.org/10.2136/sssaj1980.03615995004400050002x>.
- Wang, S., Ruspiñi, L.C., Ören, P.E., Van Offenwert, S., Bultreys, T., 2022. Anchoring multi-scale models to micron-scale imaging of multiphase flow in rocks. *Water. Resour. Res.* 58 (1). <https://doi.org/10.1029/2021wr030870>.
- Wang, S., Vafai, K., Mukhopadhyay, S., 2014. Two-phase CO₂ migration in tilted aquifers in the presence of groundwater flow. *Int. J. Heat. Mass Transf.* 77, 717–729. <https://doi.org/10.1016/j.ijheatmasstransfer.2014.06.019>.
- Wang, Y.D., Chung, T., Rabbani, A., Armstrong, R.T., Mostaghimi, P., 2021. Fast direct flow simulation in porous media by coupling with pore network and Laplace models. *Adv. Water. Resour.* 150. <https://doi.org/10.1016/j.advwatres.2021.103883>.
- Zhang, L., Guo, B., Qin, C., Xiong, Y., 2024. A hybrid pore-network-continuum modeling framework for flow and transport in 3D digital images of porous media. *Adv. Water. Resour.* 190. <https://doi.org/10.1016/j.advwatres.2024.104753>.
- Zhao, X., Shi, B., Wang, X., Zhao, J., Jiang, F., Qin, C.-Z., 2025. Modeling of permeability and formation factor of carbonate digital rocks: dual-pore-network and pore-network-continuum models. *Transp. Porous. Media* 152 (6). <https://doi.org/10.1007/s11242-025-02177-1>.